Nanoscale

PAPER

View Article Online
View Journal

Cite this: DOI: 10.1039/d5nr04968g

Thickness-driven phase selection for epitaxial helical tellurium on a van der Waals superconductor

Shuangxiang Wu,†[a,b,c] Zhanbo Fang,†[a,b,c] Yu Wang,[a,b,c] Zhiyuan Fan,[a,b,c] Cheng Jia[d] and Hui Zhang*[a,b,c]

Received 25th November 2025,
Accepted 26th March 2026

DOI: 10.1039/d5nr04968g

rsc.li/nanoscale

The unique chiral structure and strong spin–orbit coupling of helical Te make it a compelling platform for realizing novel topological quantum phenomena through van der Waals (vdW) heterostructures. However, progress has been hindered by a lack of precise control over the structural phase and interface quality of Te during ultrathin film growth. Here, we demonstrate a robust pathway for synthesizing helical Te on the superconductor $NbSe_2$, governed by a thickness-driven phase selection mechanism. Using scanning tunneling microscopy (STM), we show that Te initially forms a kinetically trapped single-layer (1L) stripe phase. When the local thickness surpasses a critical two-layer (2L) threshold, the film spontaneously transforms into epitaxial helical Te at room temperature (RT), with the 2L islands serving as nucleation centers. Combined STM and cross-sectional scanning transmission electron microscopy (STEM) analyses confirm an atomically abrupt Te/$NbSe_2$ vdW interface and identify a robust commensurate epitaxial relationship. This discovery provides a reproducible route to high-quality Te/superconductor heterostructures, providing a platform for future investigations into the interplay between structural chirality and superconducting proximity effects.

Introduction

The atomic-scale engineering of two-dimensional (2D) materials and their van der Waals (vdW) heterostructures offers a powerful paradigm for designing next-generation electronics and quantum devices. Tellurium (Te) is unique for its quasi-one-dimensional crystal structure, composed of chiral helical atomic chains.[1,2] This intrinsic anisotropy and chiral nature give rise to remarkable properties, including high carrier mobility for field-effect transistors,[3,4] a thickness-tunable band gap suitable for broadband optoelectronics,[5,6] and strong nonlinear optical responses.[7–10] Beyond conventional device properties, the helical structure of Te places it at the intersection of chirality and topological physics. It acts as a Weyl semiconductor, with magnetotransport signatures consistent with a chiral anomaly.[11] Recently, the integration of chiral structures with superconductors has emerged as a promising strategy for inducing unconventional superconducting pairing.[12–15] To explore such exotic physical phenomena in helical Te, integrating it with a superconductor *via* a pristine, crystalline interface is a critical prerequisite.

While various techniques have been developed to fabricate helical Te films, traditional growth methods often lack precise thickness control in the ultrathin limit and face challenges in realizing the high-quality interfaces required for superconducting proximity. Molecular beam epitaxy (MBE) is ideally suited for creating pristine, electronically transparent interfaces, yet the choice of substrate is paramount. MBE growth on graphene yields helical films composed of misoriented domains,[5,16] whereas growth on highly oriented pyrolytic graphite (HOPG) stabilizes a β phase rather than the bulk helical structure.[17,18] On the vdW superconductor $NbSe_2$, previous MBE studies have resulted in the helical phase forming in coexistence with a mixture of competing metastable structures.[19] The origin of this complexity is illuminated by density functional theory (DFT) calculations, which reveals multiple competing phases in ultrathin Te and predict a thickness-dependent selection rule, wherein the helical phase becomes stable only at two layers and above.[6,17] These calculations suggest that precise thickness control is critical for determining the structural phase of ultrathin Te films. However, experi-

[a]International Center for Quantum Design of Functional Materials (ICQD), Hefei National Research Center for Physical Sciences at the Microscale, University of Science and Technology of China, Hefei, Anhui 230026, China.
E-mail: huiz@ustc.edu.cn
[b]Hefei National Laboratory, University of Science and Technology of China, Hefei 230088, China
[c]Department of Physics, University of Science and Technology of China, Hefei 230026, China
[d]Institute of Quantum Materials and Physics, Henan Academy of Sciences, Zhengzhou 450046, China
†These authors contributed equally to this work.

mental validation of this pathway and the establishment of a well-defined epitaxial interface remain elusive.

Here, we uncover a thickness-driven phase selection mechanism for ultrathin Te grown *via* MBE on $NbSe_2$. We find that Te initially forms a kinetically trapped striped 1L phase. However, once the local thickness exceeds a critical threshold of 2L, the film spontaneously transforms into the thermodynamically stable helical-chain phase. This transition results in helical islands that are uniformly aligned with the substrate crystallographic axes. Through combined scanning tunneling microscopy (STM) and scanning transmission electron microscopy (STEM), we demonstrate the formation of an atomically abrupt vdW interface. Furthermore, we reveal a well-defined epitaxial registry driven by lattice commensurability, evidenced by large-scale moiré superlattices. This discovery provides a controllable route to fabricating high-quality chiral Te/superconductor heterostructures, establishing a promising platform for exploring the structural integration and electronic coupling at the limit of chirality–superconductivity interfaces.

Materials and methods

Sample growth and STM characterization

Sample growth and characterization were performed in a commercial MBE-STM system (Unisoku) with a base pressure better than 5×10^{-10} mbar. 2H-$NbSe_2$ single crystals were cleaved at room temperature (RT, ≈ 300 K) in the preparation chamber after degassing at 570 K for at least one hour. High-purity Te (Alfa Aesar, 99.999%) atoms were evaporated from a standard Knudsen cell onto the $NbSe_2$ surface held at RT. Immediately after deposition, the samples were transferred *in situ* to the STM chamber; all STM measurements were performed at 78 K. A polycrystalline PtIr tip was used as the STM probe and was characterized on a standard Au(111) surface prior to measurements.

TEM sample preparation

Cross-sectional STEM samples were prepared by a dual-beam focused ion beam (FEI Helios Nanolab G3) using standard lift-out procedures. STEM imaging was performed in a CEOS

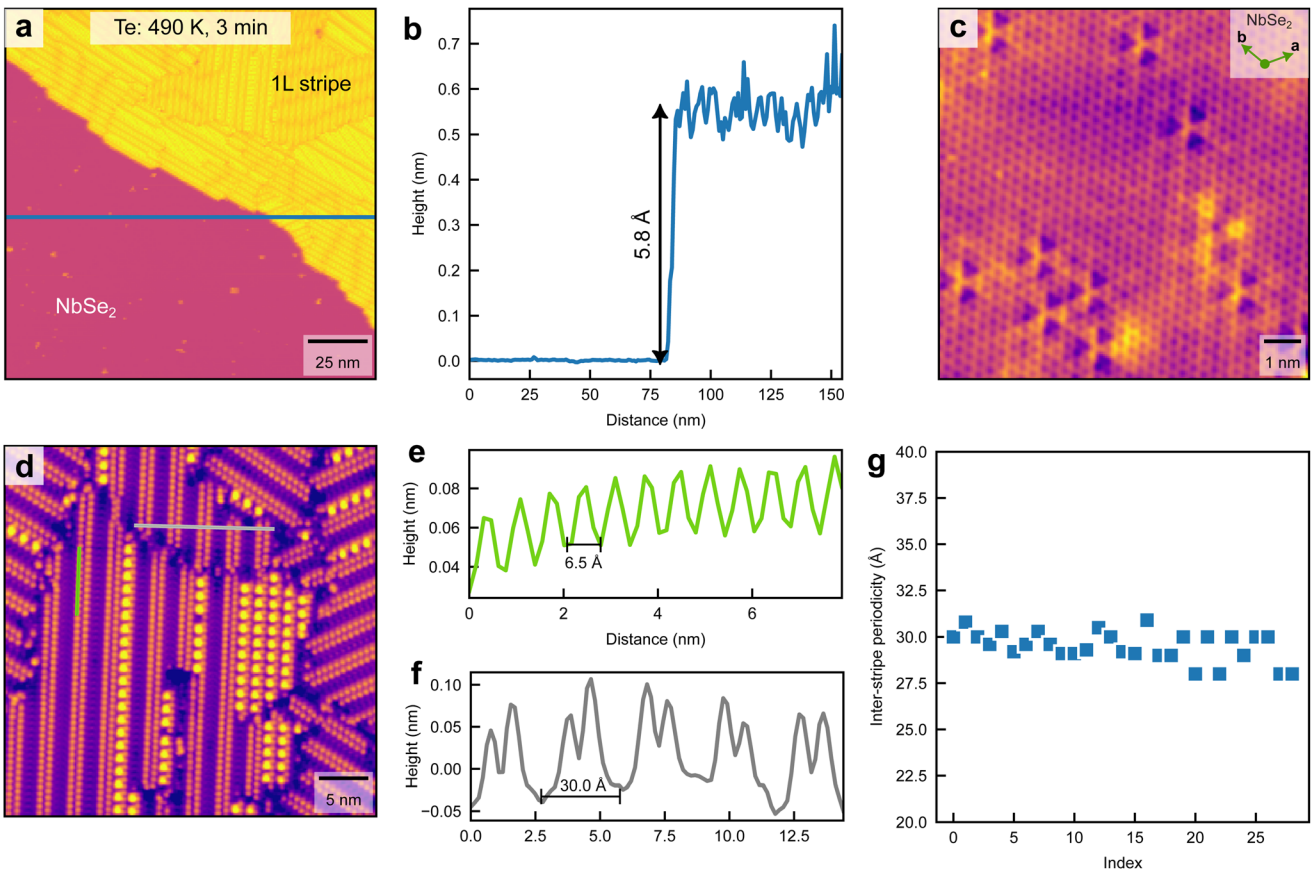

Fig. 1 Sub-monolayer striped Te on $NbSe_2$. (a) Large-area STM topography acquired after deposition for 3 minutes (nominal coverage ≈ 0.5 ML) (V_{bias} = −1.0 V, I_{set} = 50 pA). (b) Line profile along the blue line in a, confirming a uniform 1L island height of 5.8 Å. (c) Atomic-resolution STM image of the pristine $NbSe_2$ substrate; arrows indicate high-symmetry lattice directions (V_{bias} = 0.8 V, I_{set} = 400 pA). (d) High-resolution STM of a 1L Te island revealing the unidirectional striped reconstruction. On a larger scale, three equivalent domains rotated by 120° with respect to each other are observed, aligned with the substrate's high-symmetry directions. (e) Line profile along the green line in d. The intra-stripe corrugation period is ≈ 6.5 Å. (f) Line profile along the gray line in d. The inter-stripe periodicity is estimated as ≈ 30 Å. (g) Statistical scatter plot of the inter-stripe periodicity. The data were collected from d and additional large-area scan image in Fig. S1 (SI), confirming the long-range uniformity of the 1L striped phase.

probe-corrected FEI Themis TEM at an electron accelerating voltage of 300 kV with a probe convergence angle of 17.8 mrad, spatial resolution of 0.08 nm, and probe current of approximately 20 pA. The inner semi-angle for the high-angle annular dark-field (HAADF) detector was 45 mrad. HAADF-STEM images were filtered using a standard high-pass filtering method to reduce noise.

Results and discussion

Sub-monolayer striped Te stabilized by Te–Te bonding and vdW templating

With the Te source held at 490 K and a growth time of 3 minutes, the nominal Te coverage is about 0.5 monolayer (ML). Fig. 1a shows a representative STM topography. The film consists of discontinuous islands with a step height of 5.8 Å (Fig. 1b), hereafter referred to as 1L. An atomic-resolution STM image acquired on the film (Fig. 1d) reveals that the 1L Te adopts a unidirectional stripe-like structure; three equivalent orientations, separated by 120°, are observed. The stripe direction is locked to the high-symmetry directions of the $NbSe_2$ substrate, as shown by the comparison with the atomic-resolution image of bare $NbSe_2$ in Fig. 1c. Along each stripe, the intra-stripe atomic corrugation has a period of 6.5 Å (Fig. 1e), which is close to twice the $NbSe_2$ lattice constant. The typical inter-stripe spacing is about 30 Å (Fig. 1f), corresponding to approximately five times the underlying $NbSe_2$ periodicity along that direction. A statistical analysis of the inter-stripe periodicity is shown in Fig. 1g. The tight distribution around 30 Å confirms the uniform long-range order of the 1L striped phase. This stripe feature is consistent with the "zipper-like" Te structure previously reported on $NbSe_2$.[19]

The striped structure of the 1L Te points to a delicate balance of forces at the Te/$NbSe_2$ interface. Previous studies have established that substrate coupling is a critical determi-

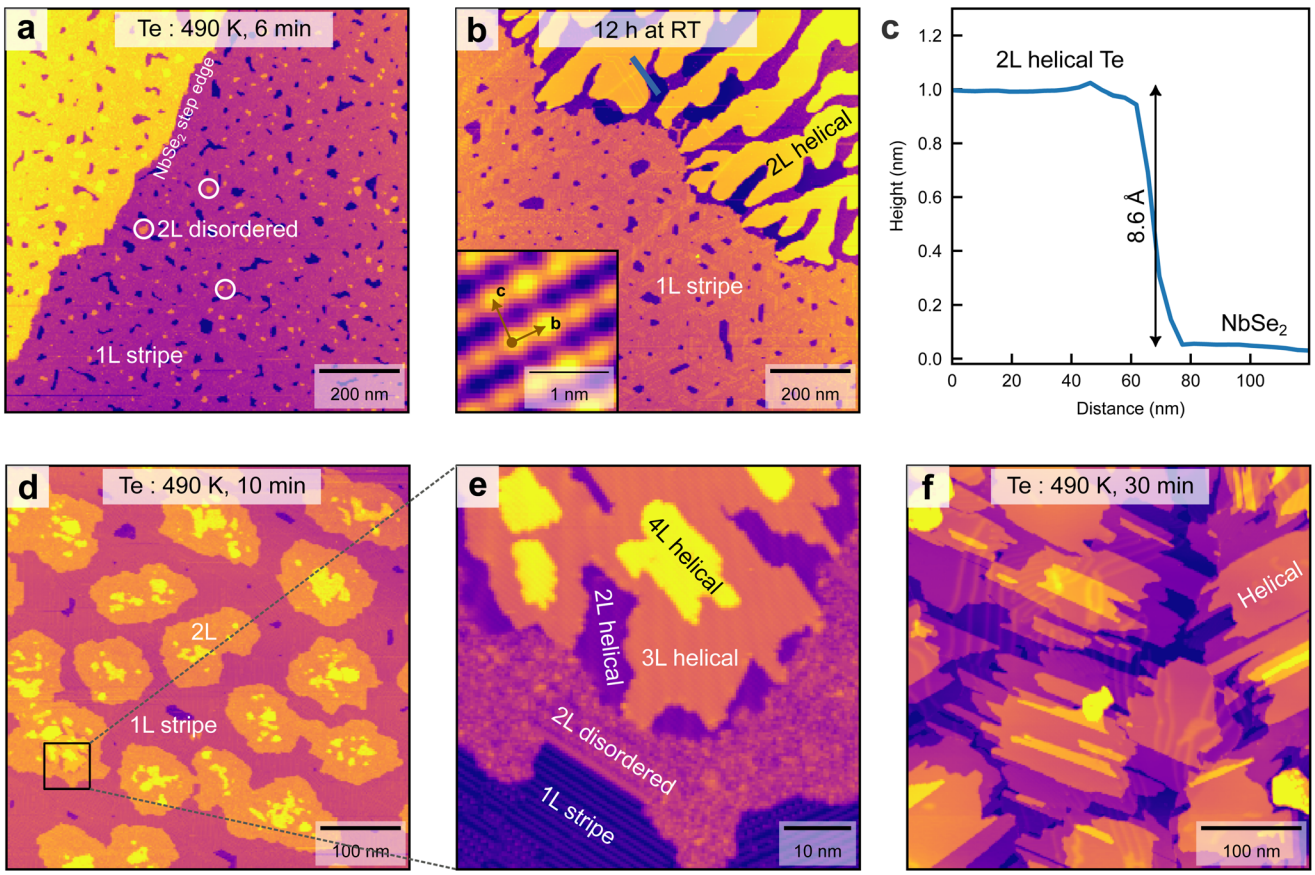

Fig. 2 Thickness-driven phase transition to helical Te at RT. (a) Large-area STM image acquired immediately after 6 minutes deposition, showing a continuous 1L striped film decorated by small 2L disordered islands (marked by white circles) (V_{bias} = −1.8 V, I_{set} = 10 pA). The yellow patch on the left corresponds to a higher substrate terrace of the underlying $NbSe_2$. (b) STM image after holding at RT for 12 hours, revealing the breakup of the 1L striped film and the emergence of large, flat-top islands (V_{bias} = −1.5 V, I_{set} = 10 pA). Inset: Atomic-resolution STM from an island terrace showing the rectangular surface lattice of trigonal helical Te on the (10$\bar{1}$0) facet, with $b \approx 4.4$ Å and $c \approx 5.9$ Å (V_{bias} = −1.0 V, I_{set} = 60 pA). (c) Line profile along the blue line in b showing a characteristic island height of ≈ 8.6 Å, consistent with the thickness of 2L helical Te. (d) Large-area STM image after 10 minutes deposition (nominal coverage ≈ 1.5 ML), showing a striped 1L film densely populated by 2L and thicker islands (V_{bias} = 1.5 V, I_{set} = 10 pA). (e) High-resolution view of a transforming 2L island, where the center has crystallized into the helical phase while the periphery remains disordered (V_{bias} = 1.5 V, I_{set} = 10 pA). (f) Large-area STM image after 30 minutes deposition, showing multilayer helical islands (V_{bias} = −0.6 V, I_{set} = 20 pA).

nant of ultrathin Te phase selection. On metals with strong chemical interactions, the substrate's influence is dominant, driving Te into novel 2D structures like hexagonal or rectangular lattices.[20–23] Conversely, on weakly interacting vdW surfaces like graphene, Te–Te interactions dominate, forming stable helical structures in randomly oriented domains.[5,16] The $NbSe_2$ surface occupies an intermediate regime. It provides a weakly interacting but structurally corrugated template. While this anisotropic potential directs the alignment of Te atoms (Fig. 1d), it cannot override the strong propensity for 1D chain formation. The resulting striped phase represents a structural compromise between these competing factors, allowing Te chains to form while locking into a unidirectional alignment dictated by the substrate.

Thickness controlled phase transition at RT

The sub-monolayer film shown in Fig. 1a exhibited no discernible changes in morphology or structure after being held at RT for over 24 hours. This indicates that the striped phase is kinetically trapped, with insufficient thermal energy for atoms to overcome the barrier for rearrangement or dewetting. To investigate the pathway for structural evolution, we increased the Te coverage. After a 6-minute deposition, the surface is almost completely covered by a 1L film (0.95 ML), which in turn serves as a template for second-layer growth (Fig. 2a). On this 1L film, we observe a sparse distribution of small islands (0.03 ML total coverage) with an average area of about 200 nm^2. These islands exhibit an apparent height of ≈ 4.5 Å and are structurally disordered (Fig. S2 in SI). We identify them as 2L islands.

A remarkable evolution unfolds upon holding the sample at RT for 12 hours. As seen in the large-area STM image in Fig. 2b, the morphology has completely rearranged. The 1L striped film has become discontinuous, acting as a material reservoir for the formation of larger, well-defined islands with atomically flat terraces. Atomic-resolution STM imaging on an island terrace (inset in Fig. 2b) reveals a well-ordered rectangular surface lattice with periodicity of $b \approx 4.4$ Å and $c \approx 5.9$ Å. These values match the lattice constants of the $(10\bar{1}0)$ surface of helical Te,[5] confirming that the island adopts the helical phase. The 2L helical islands exhibit a single preferred in-plane orientation within the field of view. Crucially, a height profile (Fig. 2c) confirms these helical islands consistently protrude about 8.6 Å above the substrate, corresponding to a uniform thickness of two layers. This suggests that 2L is the critical thickness for the formation of helical Te in this system.

The starkly different RT evolution between sub-monolayer (Fig. 1a) and slightly-above-monolayer (Fig. 2a) films implies the local 2L islands play a critical role in the spontaneous structural phase transition. This is supported by the observation in Fig. 2b and Fig. S3 in SI, where residual 1L regions that failed to transform are free of any 2L islands. To further probe the mechanism, we studied the film evolution at higher coverages.

Fig. 2d shows the sample morphology after increasing the deposition time to 10 minutes. The 2L island coverage grows significantly to 0.5 ML, and the average area increases to about 10000 nm^2. Most 2L islands are decorated by additional, higher islands. Although most 2L and higher islands appear disordered, Fig. 2d captures a localized phase transformation in progress (black square). A magnified view in Fig. 2e reveals 3L and 4L islands situated on a larger 2L terrace. Notably, while the thicker 3L and 4L islands have fully converted to the stable helical phase, the transformation in the underlying 2L layer is incomplete. Specifically, the 2L area directly beneath the 3L island has also adopted the helical structure, whereas the surrounding 2L region remains disordered. This creates a striking core–shell morphology, with a "helical core" and a "disordered shell", as detailed further in Fig. S4 in SI.

After holding this sample at RT for 4 hours, both the 1L striped film and the overlying islands transformed into the helical phase. The surface is also decorated with higher, rod-like islands (see Fig. S5 in SI). Further increasing the deposition time to 30 minutes produces the morphology shown in Fig. 2f. At this stage, the surface is completely covered by large, multilayer (>4 layers) helical Te islands without RT post-annealing. The initial 1L striped and 2L disordered phases represent transient states are no longer detected.

The critical role of the 2L island is further confirmed by the contrasting thermal stability of the sub-monolayer film. The striped islands remain intact upon heating to 410 K (Fig. 3a and b). A dramatic change occurs at 450 K (Fig. 3c). Critically, instead

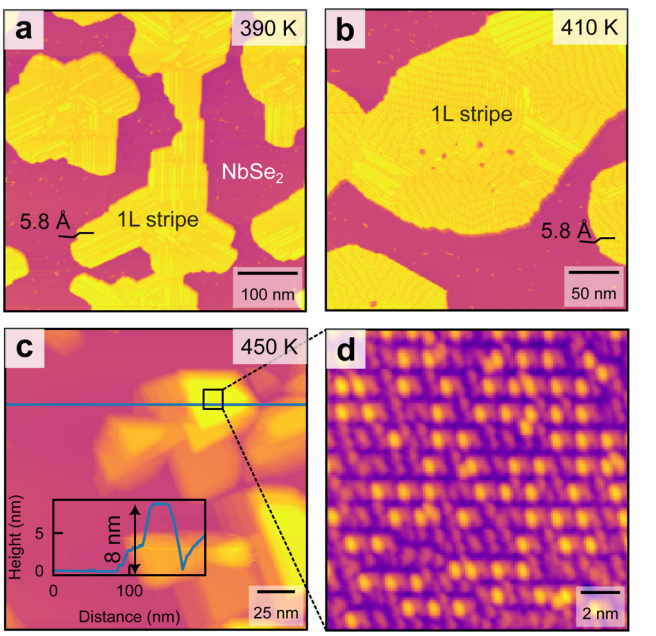

Fig. 3 Thermal instability of the striped 1L Te at sub-monolayer coverage. (a–c) Series of STM images tracking the film morphology after annealing to 390 K, 410 K, and 450 K, respectively (V_{bias} = −1.0 V, I_{set} = 60 pA). While the striped 1L islands are stable up to 410 K, they undergo dewetting at 450 K. The inset in c shows a line profile across a newly formed island, revealing a height of approximately 8 nm. (d) High-resolution STM image of a representative 3D island formed at 450 K. Its surface is disordered, confirming that the film does not convert to the helical phase upon annealing (V_{bias} = −0.8 V, I_{set} = 30 pA).

of converting to the helical phase, the striped 1L islands break apart, forming isolated and disordered 3D islands (Fig. 3d).

By employing precise thickness control, we have uncovered the mechanism of the spontaneous phase transition in ultrathin Te films. We establish that 2L islands represent the critical nucleus required for the RT transformation into the helical phase. The observed "helical core, disordered shell" morphology of these islands directly visualizes the transformation pathway, suggesting that the phase transition nucleates within the 2L regions. From these nuclei, the helical phase expands by consuming the surrounding 1L striped phase, effectively depleting the local Te reservoir to fuel the growth of thicker, stable islands. Without these 2L islands, the 1L simply undergoes dewetting into discrete 3D islands at higher temperatures. This mechanism provides direct experimental validation for theoretical predictions that the helical structure becomes the energetic ground state for films of two layers and thicker.[6,17] The electronic properties of the 2L Te islands were further characterized by scanning tunneling spectrum at 77 K. The dI/dV spectrum reveals a band gap of ≈ 0.9 eV, with the Fermi level residing in the valence band, confirming the hole-doping nature of the epitaxial Te (see Fig. S6 in the SI).

Epitaxial relationship and moiré superlattice

We next characterize the interfacial coupling to elucidate the epitaxial registry. Cross-sectional STEM (Fig. 4a) reveals an atomically abrupt interface along the Te [0$\bar{1}$10] zone axis, devoid of interdiffusion or amorphous layers. The resolved atomic columns show excellent agreement with the helical chain model, confirming a high-quality van der Waals contact.

To determine the in-plane lattice alignment, we performed atomic-resolution STM measurements. Fig. 4b compares the

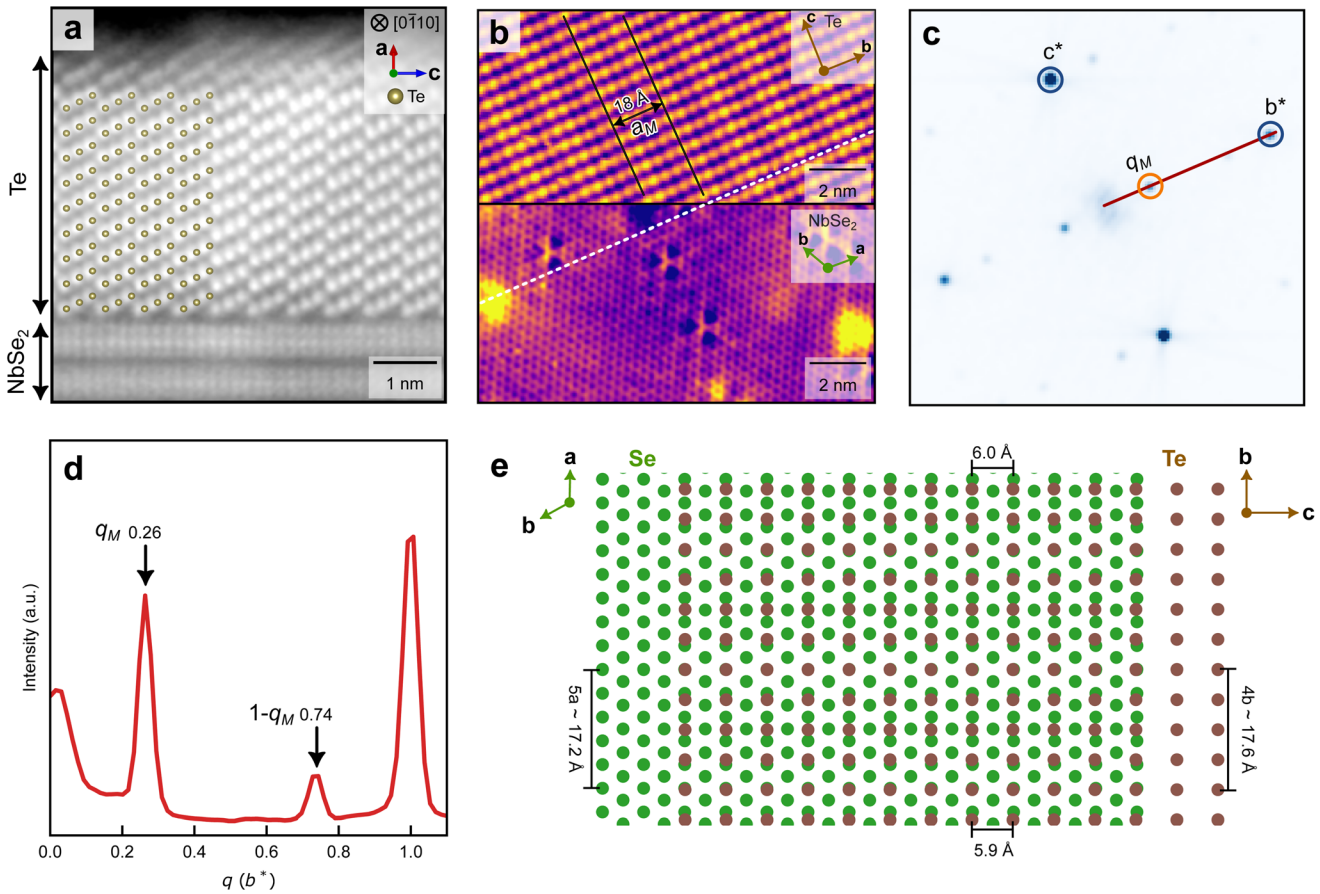

Fig. 4 Atomic-scale characterization of the interface registry and superlattice modulation. (a) Cross-sectional STEM image of a ≈4 nm Te/$NbSe_2$ heterostructure viewed along the Te [0$\bar{1}$10] direction. Atomic models of the Te helical chains are overlaid for guidance. The image confirms an atomically abrupt vdW interface. (b) Comparison of atomic-resolution STM images of Te (top panel, V_{bias} = −1 V, I_{set} = 20 pA) and $NbSe_2$ (bottom panel, V_{bias} = 0.8 V, I_{set} = 400 pA) acquired with a fixed scan orientation. Note that the *b* direction of Te is aligned parallel to the *a* direction of $NbSe_2$. A one-dimensional moiré modulation with a period of ≈ 18 Å is observed on the Te surface. (c) FFT of the Te atomic image (top panel in b). The reciprocal lattice vectors *b** and *c** are labeled. The moiré superlattice modulation is marked as q_M. (d) Line profile of the FFT intensity along the red line in c, with the wave vector (q) normalized to *b**. The moiré modulation peak is located at $q_M \approx 0.26$, corresponding to a periodicity of roughly 4b. (e) Lattice superposition simulation of the interface between hexagonal $NbSe_2$ (green Se atoms) and the rectangular Te lattice (brown atoms), constructed based on the epitaxial relationship in b. Along the transverse direction, the Te *c*-axis (≈ 5.9 Å) is nearly commensurate with 2× the $NbSe_2$ row spacing (≈ 6.0 Å). The observed moiré pattern arises along the longitudinal direction from the near-commensurability condition: $4 \times b_{Te} \approx 5 \times a_{NbSe_2}$. The simulation well reproduces the periodicity observed in b.

atomic lattices of the Te surface (top panel) and the underlying $NbSe_2$ (bottom panel), acquired consecutively from the same scan area (Fig. 2b) with a fixed scan angle. The images reveal an orientational locking where the *b*-axis of Te is parallel to the *a*-axis of $NbSe_2$. Notably, a distinct one-dimensional moiré pattern with a periodicity of ≈ 18 Å is resolved along the Te *b*-axis. This modulation exhibits pronounced long-range uniformity, as evidenced by the large-scale STM characterization shown in Fig. S7 (SI).

To quantify this periodicity, we performed Fast Fourier Transform (FFT) analysis on the Te atomic image (Fig. 4c). Besides the fundamental Bragg peaks of Te (b^* and c^*), distinct satellite peak (marked as q_M) corresponding to the moiré modulation is clearly visible. The line intensity profile along the b^* direction (Fig. 4d) identifies the moiré wavevector at $q \approx 0.26b^*$. In real space, this corresponds to a periodicity of $\approx 4b_{Te}$, which arises from the commensurability of 4 Te unit cells with 5 substrate unit cells (4×4.4 Å $\approx 5 \times 3.4$ Å).

This epitaxial model is further validated by the lattice simulation shown in Fig. 4e. A superposition model constructed with hexagonal Se and rectangular Te lattices well reproduces the experimental features. In the orthogonal direction, the Te *c*-axis (≈ 5.9 Å) naturally aligns with the $NbSe_2$ lattice, spanning two atomic rows of the substrate (2× row spacing ≈ 6.0 Å). The establishment of such bi-axial commensurability effectively minimizes interfacial strain energy, stabilizing the unidirectional growth of helical Te on $NbSe_2$.

Conclusions

In conclusion, we have established a thickness-driven phase selection mechanism for the synthesis of ultrathin helical Te on $NbSe_2$ substrate. By combining STM and STEM imaging, we demonstrated that sub-monolayer growth yields a kinetically trapped striped phase, while exceeding a 2L critical thickness triggers a spontaneous transformation into the thermodynamically stable helical structure at RT. We identified that 2L islands correspond to the critical thickness and serve as the nucleation centers for the phase transition, providing a microscopic pathway. Furthermore, we have systematically verified the epitaxial nature of the helical phase, revealing a robust crystallographic locking driven by lattice commensurability between the Te chains and the underlying superconductor. This thickness-controlled synthesis strategy, yielding high-quality, uniaxially oriented chiral films, establishes a robust material platform for atomic-scale engineering of interfaces between chiral crystals and superconductors, opening new avenues for designing helical-chain based quantum devices.

Author contributions

S. Wu: investigation, formal analysis, writing – original draft. Z. Fang: investigation, writing – review & editing. Y. Wang: investigation. Z. Fan: investigation. C. Jia: formal analysis. H. Zhang: conceptualization, supervision, project administration, funding acquisition, writing – review & editing.

Conflicts of interest

The authors declare no conflict of interest.

Data availability

The data supporting this article have been included in the manuscript.

Supplementary information (SI): STM image of the rotational domains of the 1L stripe phase (Fig. S1); STM image of the disordered 2L island (Fig. S2); large-area STM topography from a different region on the same sample as shown in Fig. 2b (Fig. S3); zoomed-in STM image of the helical-core/disordered-shell morphology during transformation (Fig. S4); STM image of the 1.5ML sample after holding at RT for 4 hours (Fig. S5); typical dI/dV spectrum acquired on a 2L Te island at 77 K (Fig. S6); large-scale STM characterization of the moiré pattern (Fig. S7). See DOI: https://doi.org/10.1039/d5nr04968g.

Acknowledgements

This work was supported by the National Key Research and Development Program of China (Grant No. 2023YFA1406300), the Quantum Science and Technology-National Science and Technology Major Project (Grant No. 2021ZD0302800), the National Natural Science Foundation of China (Grant No. 12488101), Anhui Provincial Key Research and Development Project (Grant No. 2023z04020008), the CAS Project for Young Scientists in Basic Research (Grant No. YSBR-046).

References

1 A. von Hippel, *J. Chem. Phys.*, 1948, **16**, 372–380.
2 A. Ben-Moshe, A. da Silva, A. Müller, A. Abu-Odeh, P. Harrison, J. Waelder, F. Niroui, C. Ophus, A. M. Minor, M. Asta, W. Theis, P. Ercius and A. P. Alivisatos, *Science*, 2021, **372**, 729–733.
3 Y. Wang, G. Qiu, R. Wang, S. Huang, Q. Wang, Y. Liu, Y. Du, W. A. Goddard, M. J. Kim, X. Xu, P. D. Ye and W. Wu, *Nat. Electron.*, 2018, **1**, 228–236.
4 C. Zhao, C. Tan, D.-H. Lien, X. Song, M. Amani, M. Hettick, H. Y. Y. Nyein, Z. Yuan, L. Li, M. C. Scott and A. Javey, *Nat. Nanotechnol.*, 2020, **15**, 53–58.
5 X. Huang, J. Guan, Z. Lin, B. Liu, S. Xing, W. Wang and J. Guo, *Nano Lett.*, 2017, **17**, 4619–4623.
6 J. Qiao, Y. Pan, F. Yang, C. Wang, Y. Chai and W. Ji, *Sci. Bull.*, 2018, **63**, 159–168.

7 J. Peng, Y. Pan, Z. Yu, J. Wu, J. Wu, Y. Zhou, Y. Guo, X. Wu, C. Wu and Y. Xie, *Angew. Chem., Int. Ed.*, 2018, **57**, 13533–13537.
8 M. Amani, C. Tan, G. Zhang, C. Zhao, J. Bullock, X. Song, H. Kim, V. R. Shrestha, Y. Gao, K. B. Crozier, M. Scott and A. Javey, *ACS Nano*, 2018, **12**, 7253–7263.
9 L. Wu, W. Huang, Y. Wang, J. Zhao, D. Ma, Y. Xiang, J. Li, J. S. Ponraj, S. C. Dhanabalan and H. Zhang, *Adv. Funct. Mater.*, 2019, **29**, 1806346.
10 J. Ma, B. Cheng, L. Li, Z. Fan, H. Mu, J. Lai, X. Song, D. Yang, J. Cheng, Z. Wang, C. Zeng and D. Sun, *Nat. Commun.*, 2022, **13**, 5425.
11 N. Zhang, G. Zhao, L. Li, P. Wang, L. Xie, B. Cheng, H. Li, Z. Lin, C. Xi, J. Ke, M. Yang, J. He, Z. Sun, Z. Wang, Z. Zhang and C. Zeng, *Proc. Natl. Acad. Sci. U. S. A.*, 2020, **117**, 11337–11343.
12 Z. Wan, G. Qiu, H. Ren, Q. Qian, Y. Li, D. Xu, J. Zhou, J. Zhou, B. Zhou, L. Wang, *et al.*, *Nature*, 2024, **632**, 69–74.
13 H.-Z. Tang, Q.-F. Sun, J.-J. Liu and Y.-T. Zhang, *Phys. Rev. B*, 2019, **99**, 235427.
14 H. Alpern, E. Katzir, S. Yochelis, N. Katz, Y. Paltiel and O. Millo, *New J. Phys.*, 2016, **18**, 113048.
15 Q. Chen, A.-M. Guo, J. Liu, F. M. Peeters and Q.-F. Sun, *New J. Phys.*, 2021, **23**, 93047.
16 G. Miao, J. Qiao, X. Huang, B. Liu, W. Zhong, W. Wang, W. Ji and J. Guo, *Phys. Rev. B*, 2021, **103**, 235421.
17 Z. Zhu, X. Cai, S. Yi, J. Chen, Y. Dai, C. Niu, Z. Guo, M. Xie, F. Liu, J.-H. Cho, Y. Jia and Z. Zhang, *Phys. Rev. Lett.*, 2017, **119**, 106101.
18 J. Chen, Y. Dai, Y. Ma, X. Dai, W. Ho and M. Xie, *Nanoscale*, 2017, **9**, 15945–15948.
19 J.-J. Xian, C. Wang, Z.-M. Zhang, L. Qin, W. Ji, F.-C. Chen, X. Luo, Y.-P. Sun, W.-H. Zhang and Y.-S. Fu, *Nanoscale*, 2020, **12**, 1994–2001.
20 M. Bouaziz, W. Zhang, Y. Tong, H. Oughaddou, H. Enriquez, R. Mlika, H. Korri-Youssoufi, Z. Chen, H. Xiong, Y. Cheng and A. Bendounan, *2D Mater.*, 2020, **8**, 15029.
21 Y. Tong, M. Bouaziz, W. Zhang, B. Obeid, A. Loncle, H. Oughaddou, H. Enriquez, K. Chaouchi, V. Esaulov, Z. Chen, H. Xiong, Y. Cheng and A. Bendounan, *2D Mater.*, 2020, **7**, 35010.
22 J. Shah, H. M. Sohail, R. I. G. Uhrberg and W. Wang, *J. Phys. Chem. Lett.*, 2020, **11**, 1609–1613.
23 W. Quan, C. Hong, S. Pan, J. Hu, Q. Wu, Z. Zhang, F. Zhou, F. Zheng, Z. Zhu and Y. Zhang, *ACS Appl. Mater. Interfaces*, 2023, **15**, 16144–16152.